Supplementary Material

Advanced Spectroscopic Analysis and ^{15}N-Isotopic Labelling Study of Nitrate and Nitrite Reduction to Ammonia and Nitrous Oxide by *E. coli*

George D. Metcalfe [1], Thomas W. Smith [1,2] and Michael Hippler [1]*

[1] ***Department of Chemistry, University of Sheffield, Sheffield S3 7HF, UK***

[2] ***School of Chemical Engineering and Analytical Science, University of Manchester, Manchester M13 9PL, UK***

[*] ***Corresponding author. E-Mail: M.Hippler@sheffield.ac.uk***

Content:

S.1. Key Nitrate and Nitrite Reduction Enzymes

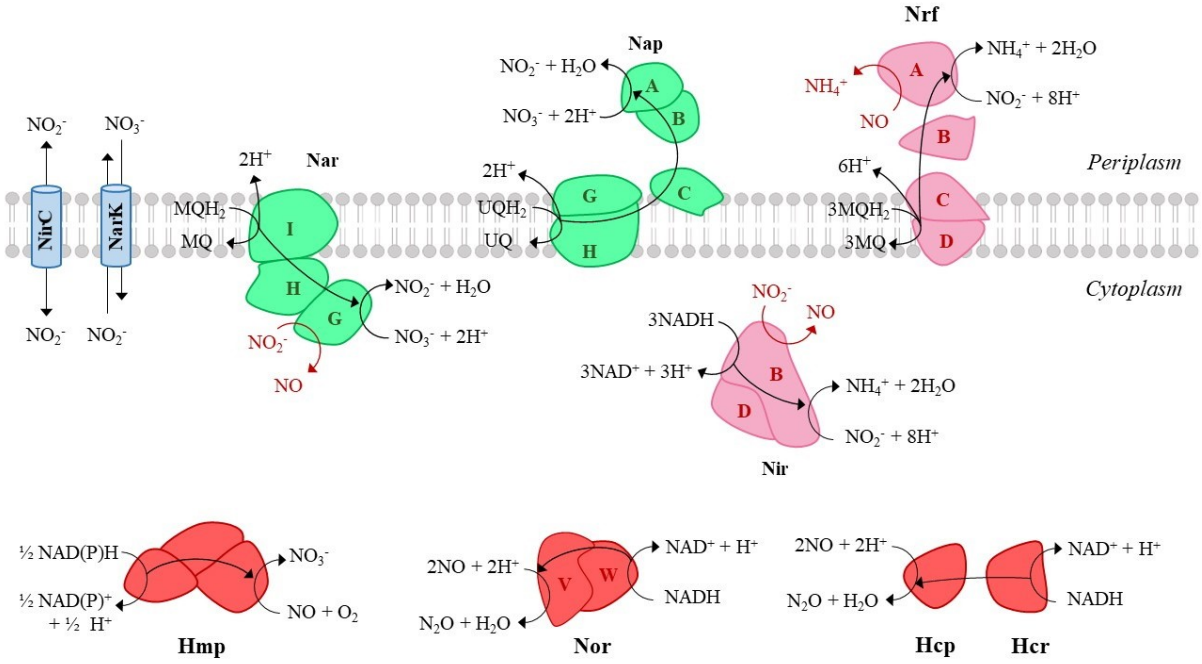

Fig. S1. The cellular locations of key enzymes during NO_3^- and NO_2^- reduction by *E. coli*, including generation or detoxification of NO by NO_3^- and NO_2^- reductases. Enzymes are displayed in boldface: **Hcp**, hybrid cluster protein; **Hcr**, NADH-dependent Hcp reductase; **Hmp**, flavohemoglobin; **NarK**, a NO_3^-/NO_2^- antiporter; **NirB**, NADH dependent NO_2^- reductase; **NirC**, a NO_2^- transporter; **NorV**, flavorubredoxin; **Nap**, periplasmic NO_3^- reductase; **Nar**, NO_3^- reductase A; **NrfA**, periplasmic NO_2^- reductase.

Fig. **S1** shows the cellular locations of key enzymes involved during *E. coli* NO_3^- and NO_2^- reduction. *E. coli* expresses three NO_3^- reductases: the respiratory NO_3^- reductases A and Z (NRA and NRZ) and the periplasmic NO_3^- reductase (Nap) [1–3]. NRA is the major anaerobic NO_3^- reductase active at high NO_3^- levels (> 2 mM) while Nap is induced by low NO_3^- levels [4]. NRZ is expressed at low levels constitutively and may function under stress-associated conditions or in an adaptive role in the transition from aerobiosis to anaerobic NO_3^- respiration [5, 6]. Formate is a physiological source of electrons for NO_3^- reduction that is oxidised to CO_2 by the NO_3^--inducible formate dehydrogenase (FdhN) and transfers electrons to the quinone pool of the membrane [2], other sources include reduced nicotinamide adenine dinucleotide (NADH), lactate and glycerol [1]. NADH-dependent cytoplasmic NO_2^- reductase (NirB) and the membrane-bound periplasmic NO_2^- reductase (NrfA) formally catalyse the six-electron reduction of NO_2^- to NH_3 instead of the one-electron reduction of NO_2^- to NO [7]. Nevertheless, *E. coli* still generates low levels of NO during anaerobic growth on NO_3^-, either from the disproportion of NO_2^- under acidic conditions or non-specific reduction by metalloproteins. NRA (in the absence of NO_3^-) [8–11], NirB [12] and NrfA [13] have all been proposed to be significant sources of NO formation. Both NO_2^- and NO are cytotoxic species and careful control of their intracellular concentration is required, either through detoxification to less reactive species or by excretion. Anaerobically, NO is detoxified by reduction to N_2O, which is comparatively non-toxic and rapidly diffuses out of the cell. Flavorubredoxin (NorV) [14], hybrid cluster protein (Hcp) [15], NirB [16] and NrfA [17] have all been proposed to have NO detoxifying activity. Flavohemoglobin (Hmp) is primarily an NO oxidase but also acts as an NO reductase

anaerobically [18]. As *E. coli* does not possess any known N_2O reductases, further reduction to N_2 is not expected to occur. However, there is some evidence that N_2 might be produced under some conditions by a yet unknown mechanism [19].

S.2. M9 Formulation

Our entire M9 formulation is listed below. To this base formulation we supplemented 10 mM $K^{15}NO_3$ (10 mM, 98 atom % ^{15}N, Sigma Aldrich) and/or 5 mM KNO_2 (either ^{14}N or ^{15}N).

- 48 mM Sodium phosphate dibasic
- 30 mM Glucose
- 22 mM Potassium phosphate monobasic
- 18 mM Ammonium chloride
- 8.5 mM Sodium chloride
- 1 mM Magnesium sulphate
- 1 mM Thiamine hydrochloride
- 300 µM Calcium chloride
- 134 µM Tetrasodium EDTA
- 56.6 µM Boric acid
- 31 µM Iron(III) chloride
- 9 µM Nickel chloride hexahydrate
- 6.2 µM Zinc chloride
- 4 µM Biotin
- 4 µM Sodium selenite
- 3.2 µM Sodium molybdate dihydrate
- 2.7 µM Cobalt(II) chloride hexahydrate
- 1.3 µM Manganese(II) chloride tetrahydrate
- 0.2 µM Copper(II) sulphate

S.3. FTIR Spectroscopy of CO_2 and Ethanol

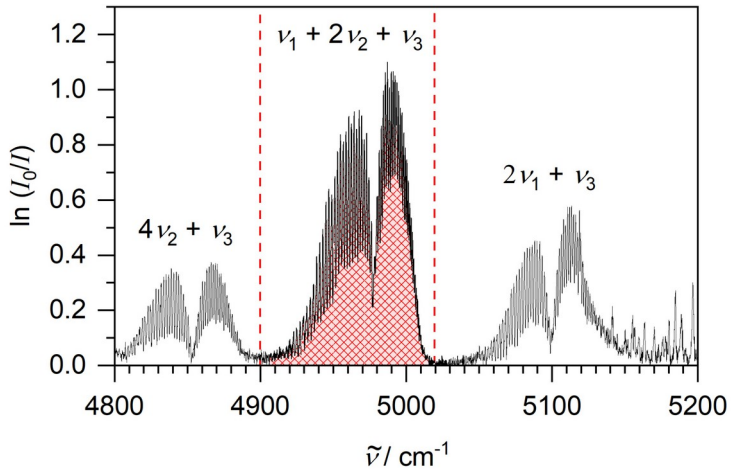

Fig. S2. Experimental White cell FTIR Spectrum of the CO_2 ($2\nu_1+\nu_3$) Fermi triad. The CO_2 partial pressure was 100 mbar calculated from the integral of the shaded $\nu_1+2\nu_2+\nu_3$ band.

Production of CO_2, ethanol and N_2O was quantified by gas-phase FTIR spectroscopy (Mattson Research Series, 0.4 cm^{-1} spectral resolution, 1000 - 7000 cm^{-1} range, liquid N_2 cooled MCT detector) with a home-built multiple-pass absorption White cell [20]. N_2O spectral bands and fitting procedures are described in the main text. Fig. **S2** shows an experimental spectrum of the ($2\nu_1+\nu_3$) Fermi triad of CO_2, corresponding to 100 mbar in 1 atm. The integral of the red-shaded $\nu_1 + 2\nu_2 + \nu_3$ band (4920 - 5015 cm^{-1}, ν_0 = 4978 cm^{-1}) was compared with a reference spectrum taken from the PNNL database to calculate CO_2 partial pressure [21]. PNNL spectra corresponded to 1 ppm-meter of a species and so were scaled to 6 m, the folded pathlength of our White cell.

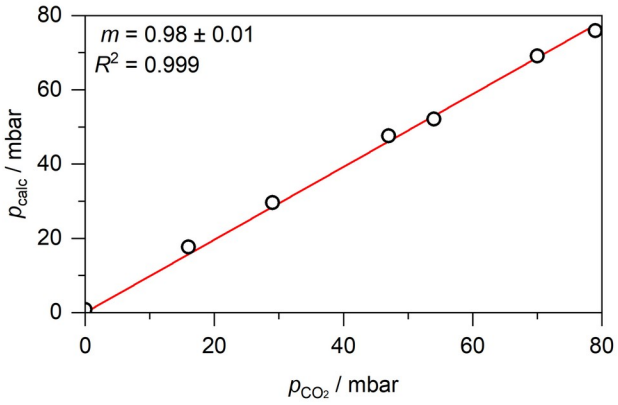

Fig. S3. White cell calibration plot showing the calculated CO_2 partial pressure as a function of CO_2 partial pressure, assuming a folded pathlength of 6 m.

Fig. **S3** shows the excellent linearity between the calculated partial pressures of CO_2 (p_{calc}) and CO_2 in 1 atm air. This confirmed the 6 m folded pathlength of our White cell. Non-linearity was observed at CO_2 partial pressures greater than 100 mbar due to the $\nu_1 + 2\nu_2 + \nu_3$ exceeding a peak absorbance of unity. This was not an issue for our experiments displayed in the main text as CO_2 produced by *E. coli* did not exceed 100 mbar, under our conditions.

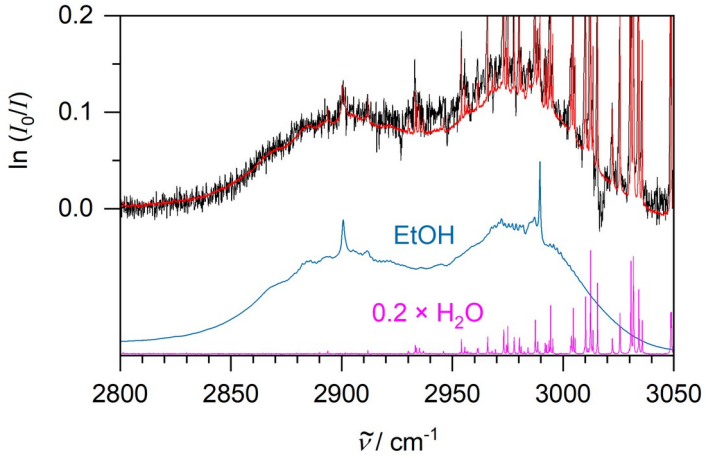

Fig. S4. In black, an experimental White cell FTIR spectrum of 63 ppm ethanol (5.1 mM in solution). In red, the sum of the fitted ethanol and water models shown below the overlaid spectra. The water model is divided by five for clarity due to the intense lines.

Fig. **S4** shows the fitting procedure to obtain ethanol partial pressure. In the C-H stretching region, the broad ethanol peak overlapped with sharp water lines. Using a least-squares fitting routine, model spectra of 1 ppm ethanol and water taken from the PNNL database were fitted to experimental spectra, returning a multiplier equal to the partial pressure of ethanol. Using Henry's law, this partial pressure was converted to concentration in solution.

S.4. Cavity Enhanced Raman Spectroscopy (CERS)

S.4.1. Experimental Details of CERS

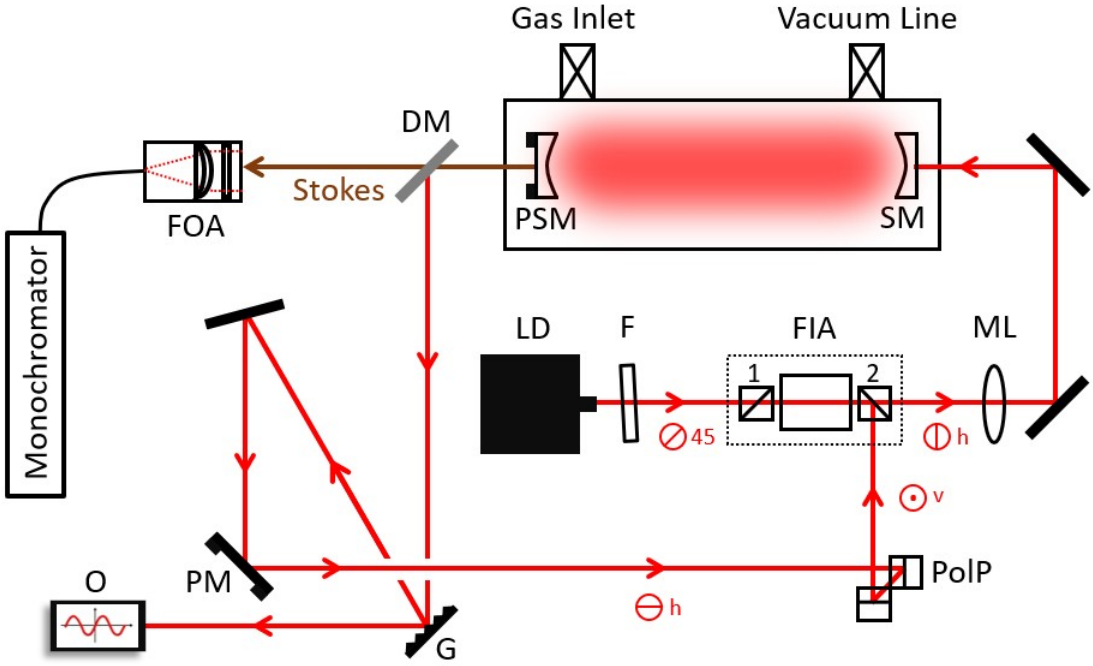

Fig. S5. Scheme of the experimental CERS setup. **DM**, dichroic mirror; **F**, filter; **FIA**, Faraday isolator assembly; **FOA**, fibre optical assembly; **G**, grating; **LD**, laser diode; **ML**, mode matching lens; **O**, oscilloscope; **PM**, mirror on a piezomount; **PolP**, polarization plane turning prism pair; **PSM**, supermirror on a piezomount; **SM**, supermirror.

The experimental CERS setup (Fig. **S5**) has been described before [22–25], but contains several modifications. A 40 mW 636 nm single-mode cw-diode laser (HL63133DG) is coupled *via* a short-pass filter, a Faraday isolator and a mode matching lens into a linear optical cavity composed of two highly reflective mirrors (Newport SuperMirrors, R > 99.99 %). If the laser wavelength matches the cavity length, then an optical resonance builds up optical power inside the cavity by up to 3 orders of magnitude, enhancing the Raman signals. The enhancement can be clearly seen in Fig. **S6** showing a photograph that was taken when the cavity was opened for cleaning. In the present simplified setup, no active mode matching was attempted; the diode laser current was rather modulated periodically to allow periodic mode matching which is then re-enforced by optical feedback. After the cavity, a dichroic mirror separates leftover excitation light from Raman signals which are coupled into a round-to-linear glass fibre bundle (7 x Ø105 µm) and transferred to the monochromator. Remaining excitation light is fed back to the diode for frequency stabilization to match the laser wavelength to the cavity. In the feedback loop there are a grating (G), a piezo-mounted mirror (PM) and a set of 2 prisms (PolP) to change the polarisation from horizontally to vertically polarised. The grating is in 1st order reflection to select just one wavelength of the possible cavity modes, to encourage single mode operation by feedback. The piezo-mirror is to adjust the feedback loop length to the laser wavelength ('phase matching'). In a simplification, we are not using active phase matching but apply a periodic change which will lock the laser periodically to a resonance. In the setup, only one Faraday isolator is used. The original 45° polarised diode laser light will be horizontally polarised after the isolator. To

allow feeding light back to the diode *via* the rejection port of the Faraday isolator, it has to be vertically polarised which is achieved by the prism pair rotating the polarisation.

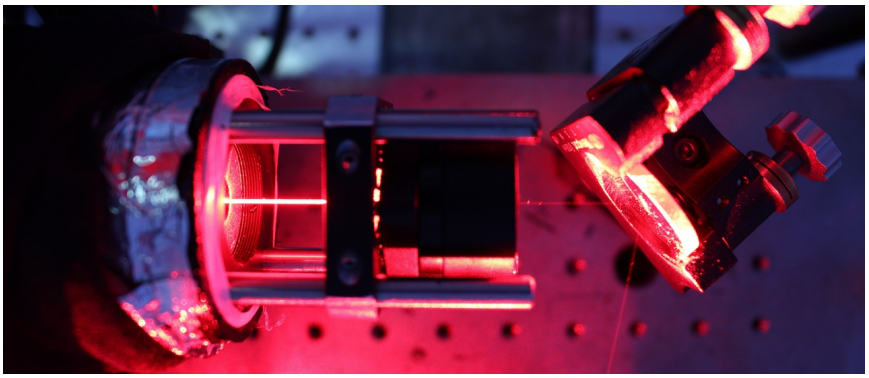

Fig. S6. Photograph taken of the inside of the cavity while open for cleaning, clearly showing the power enhancement of the red laser beam inside the cavity.

S.4.2. Spectral Fitting Procedures and Calibration Plots

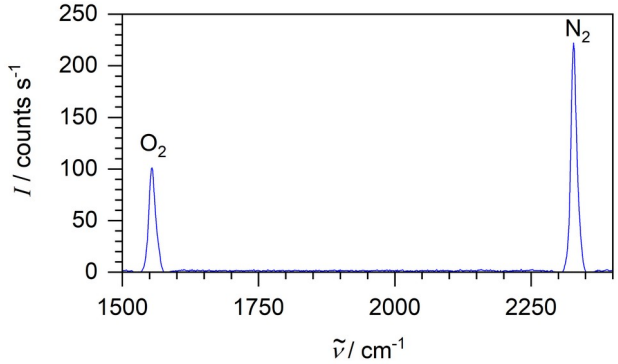

Fig. S7. CERS spectrum of 1 atm air (210 mbar O_2 and 790 mbar N_2).

Fig. **S7** shows a CERS spectrum of air, with the *Q*-branches of the O_2 and N_2 vibrational fundamentals visible. Fig. **S8** shows a CERS spectrum of 140 mbar each of H_2 and CO_2, taken during a bacterial anaerobic fermentation experiment.

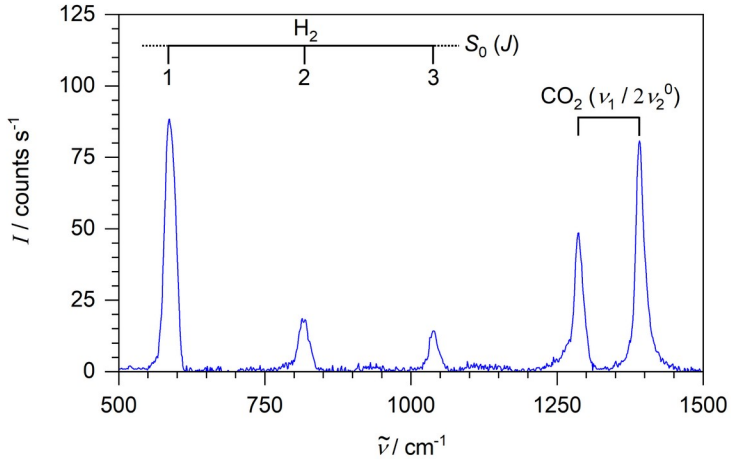

Fig. S8. CERS spectrum of H_2 and CO_2 (140 mbar of each).

The area of the *S*(1) rotational peak of H_2 was divided by the area of the *Q*-branch of N_2 (corresponding to 1 atm in anaerobic experiments) in order to obtain H_2 partial pressures after a calibration. Using known partial gas pressures, a calibration was made for H_2 showing excellent

linearity, see Fig. **S9**. A similar procedure has been applied to CO_2; the calibration also shows excellent linearity, see Fig. **S9**.

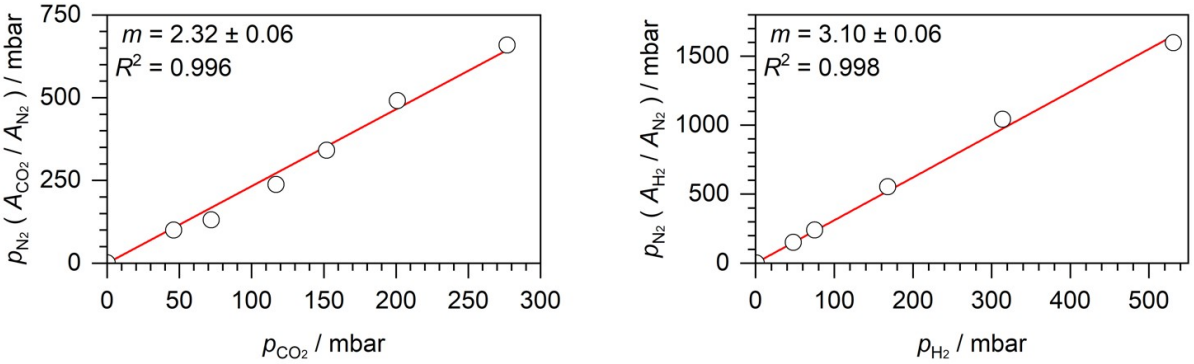

Fig. S9. CO_2 and H_2 calibration plots.

S.5. Liquid Phase Raman Spectroscopy

S.5.1. Experimental Details of the Home-built Raman Spectrometer

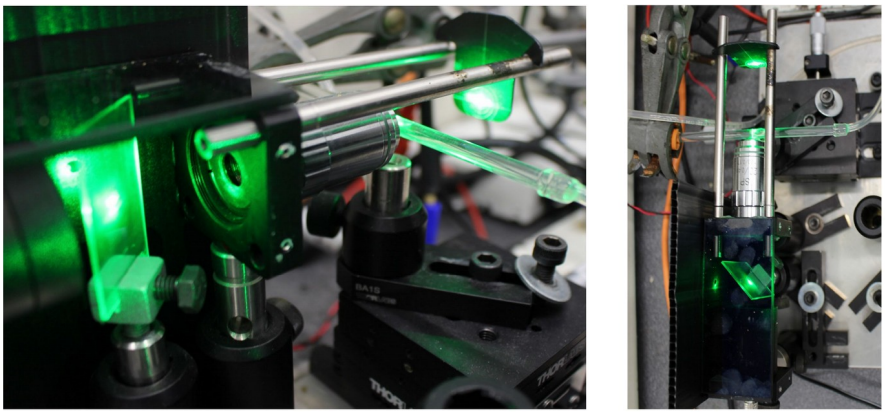

Fig. S10. Photographs of the home-built spectrometer set-up, showing the laser beam path through the mirror and the microscope objective to the sample. Left: side view; right: top view.

The home-built Raman spectrometer was first described in ref. [26] and modified later as described in refs. [20, 27]; key components of the monochromator and the camera have been described in refs [22, 23]. Briefly, a frequency doubled Nd:YAG laser, 532.2 nm, 20 mW (Lasos, GL3dT) emits green excitation light that is turned by 90° by a small mirror and coupled into a microscope objective. The small mirror was a 2 mm × 3 mm oval film deposited in the centre of a glass slide so as not to take away too much of the Raman backscattered light. The microscope objective is a 20x, 0.50 NA achromatic objective (OptoSigma, 028-0220) with a large clear aperture (8.2 mm). The objective focused the laser light very tightly at 2 mm distance from the objective front into the glass tube, as well as collimating the resulting Raman backscattered light. The sample volume is essentially the focus volume with an estimated spatial resolution below 100 µm. The backscattered light passed through the glass slide and was coupled into a lens and transmitted to the monochromator (Shamrock SR-750-A) equipped with 1200 l/mm grating, 750 nm blaze, and CCD camera (Andor i-Dus DU420A-OE at –80 °C). The grating provided a 880 cm-1 spectral range at about 0.8 cm-1 resolution. After wavenumber calibration, Raman peak position accuracy is estimated to be ± 3 cm-1 .

Raman reference spectra were obtained in borosilicate NMR test tubes. A scheme of the Raman setup is part of Fig. 2 in the main text. In addition, see Fig. **S10** for two photos of the Raman spectrometer.

S.5.2. Spectral Fitting Procedures and Calibration Plots

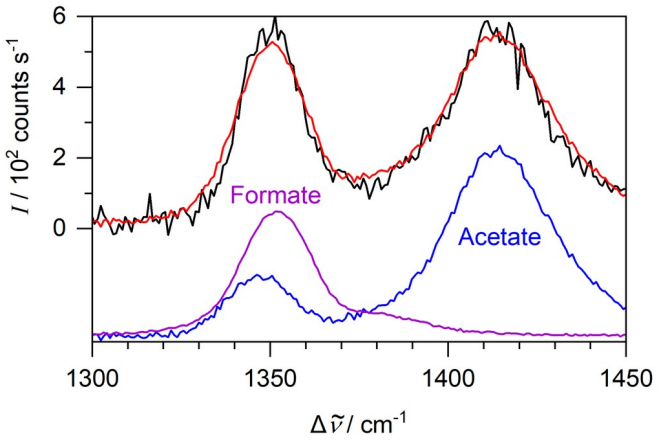

Fig. S11. In black, an experimental Raman spectrum of M9 medium containing 30 mM acetate and 10 mM formate excreted by *E. coli*. In red, the sum of the fitted acetate and formate models shown below the overlaid spectra.

As described in the main text, experimental liquid Raman spectra were fitted with the sum of model Raman spectra of pure compounds of known concentration and a linear baseline. Fig. 3 in the main text shows an example fitting procedure for NO_3^-, glucose, $H_2PO_4^-$ and HPO_4^{2-} at 825 - 1200 cm^{-1}. Fig. **S11** shows an example fit for the other species we analyse by liquid phase Raman spectroscopy, acetate and formate between 1300 - 1450 cm^{-1}, as first described in ref. [20].

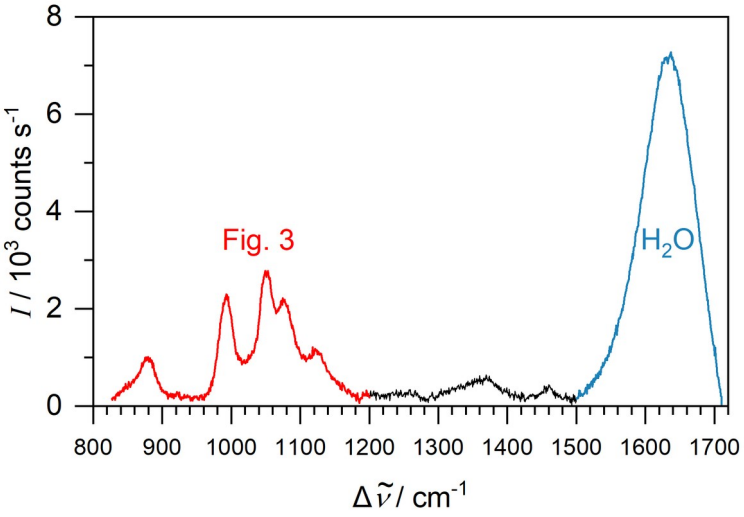

Fig. S12. The entire experimental Raman spectrum of M9 medium supplemented with 10 mM $K^{15}NO_3$ and 30 mM glucose.The water bending vibration is highlighted in blue. See the main text for Fig. 3.

The least-squares fitting procedures returned multipliers *x* that were normalised by dividing by the water area peak (bending vibration of the water solvent at 1630 cm^{-1}) to give *x*'; this normalisation was particularly relevant for our biological samples which became turbid with time. In the normalisation, the water peak was fitted by a Gaussian contour centered at 1630 cm^{-1} with FWHM

of 80 cm^{-1}. Normalisation assumed that the area of this Gaussian was the same in all solution Raman spectra because water concentrations remained the same. Fig. **S12** shows the water peak as well as the entire spectral range (830 - 1710 cm^{-1}) of a typical solution Raman spectrum. The part of the spectrum coloured red is displayed in the main text in Fig. 3.

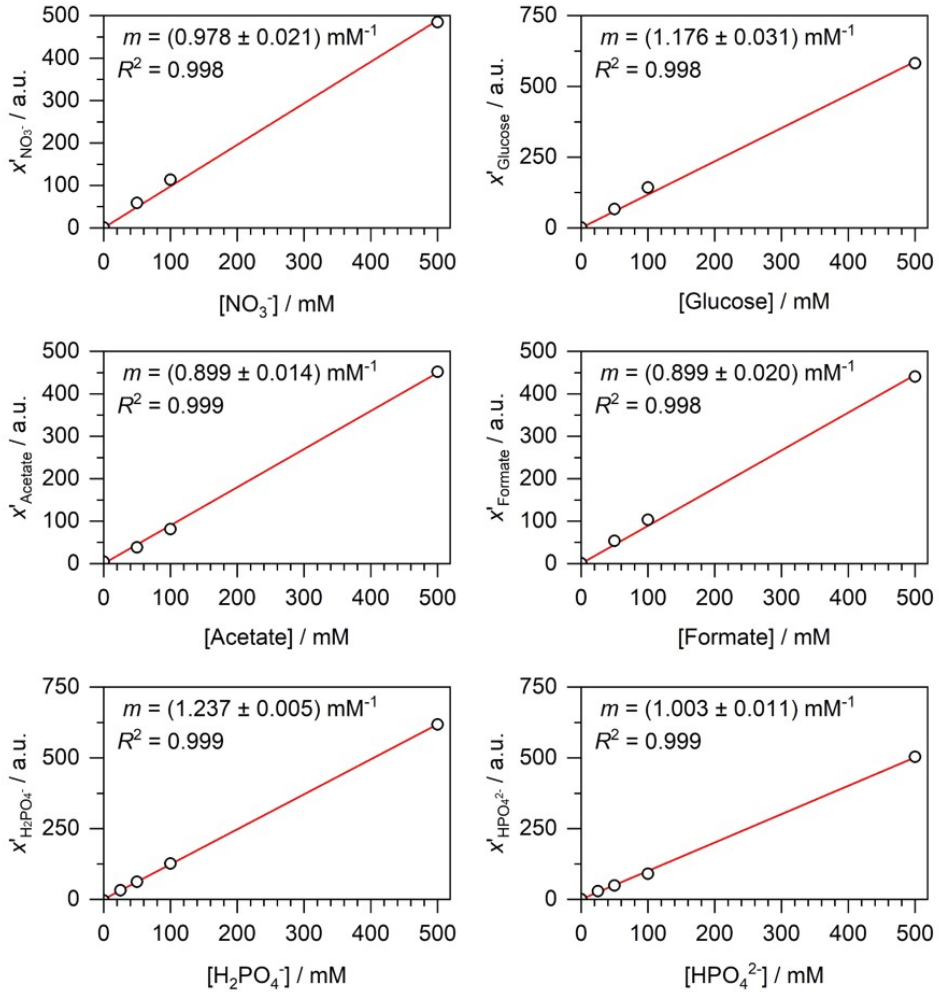

Fig. S13. Calibration plots of normalized Raman signals *x*' (in a.u.) *versus* concentration in solution for NO_3^-, glucose, acetate, formate, $H_2PO_4^-$ and HPO_4^{2-}; with linear fit lines, slopes *m* and R^2 values.

The normalized x' provides the concentration of the compound in comparison with the known concentration of the pure compound used as the model for the fit. This procedure was validated by calibration plots shown in Fig. **S13** where the concentrations of calibration solutions were determined as described above and compared with the nominal concentrations. Excellent linearity (as shown by the R^2 value) and a good dynamic range are demonstrated in all cases. m denotes the slope of the calibration curves. Error bars, as represented by the standard deviation of repeat measurements, are approximately the size of the symbols used or smaller and are therefore not included in the calibration plots.

S.6. Analysis of Bacterial Culture Samples

S.6.1. Nitrite Colorimetry

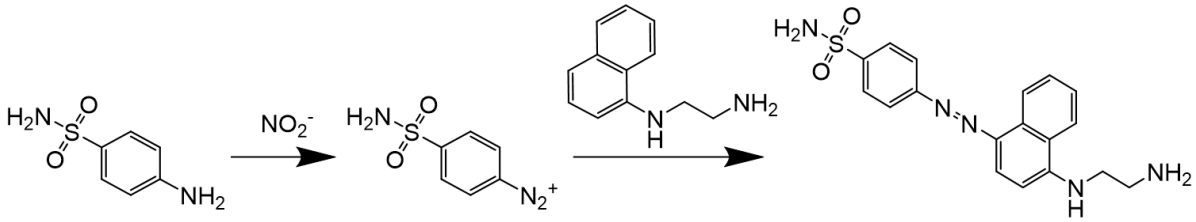

Scheme S1. The two subsequent reactions of the Griess test.

Scheme **S1** shows the two subsequent reactions of the Greiss test. First NO_2^- reacts with sulfanilamide forming a diazonium salt which then reacts in an azo coupling reaction with N-(1-napthyl)ethylenediamine forming a pink azo dye. The pink colour is shown in Fig. **S14**.

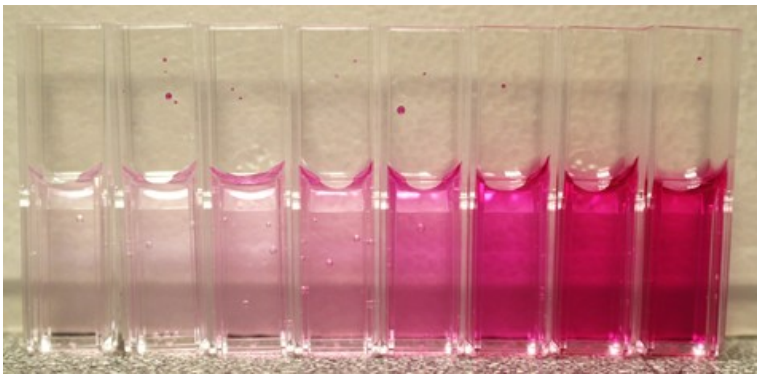

Fig. S14. The pink azo dye formed by the Griess test for NO_2^-.

By using a spectrophotometer, NO_2^- can be quantitatively determined by measuring the absorbance at 520 nm, as shown by the calibration plot in Fig. **S15**.

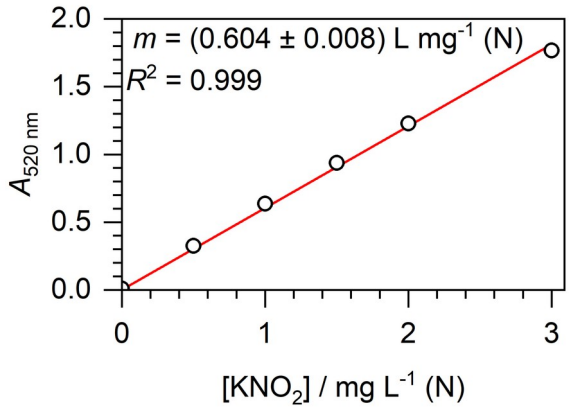

Fig. S15. NO_2^- colorimetry calibration plot.

S.6.2. $^{14}N/^{15}N$-Ammonium Analysis

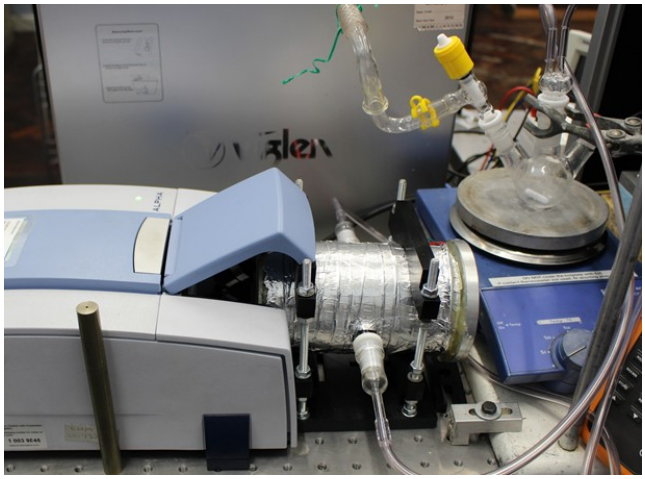

Fig. S16. The White cell (2.8 m folded pathlength) FTIR and flask setup for analysing $^{14}NH_3$ and $^{15}NH_3$.

For $^{14}N/^{15}N$ ammonium analysis of samples, 2 mL 1 M NaOH was added to 0.6 mL of sample to release ammonia gas in a flask connected to our second FTIR set-up (Bruker Alpha FTIR, 0.8 cm^{-1} spectral resolution, 350 - 7000 cm^{-1} range) also with a home-built multiple-pass absorption White cell (2.8 m pathlength), shown in Fig. **S16**. The gases were cycled using a peristaltic pump (4.5 L/h) and the solution was stirred rapidly. Spectra were recorded every 5 minutes with around 30 minutes needed before ammonia concentration peaked in the headspace.

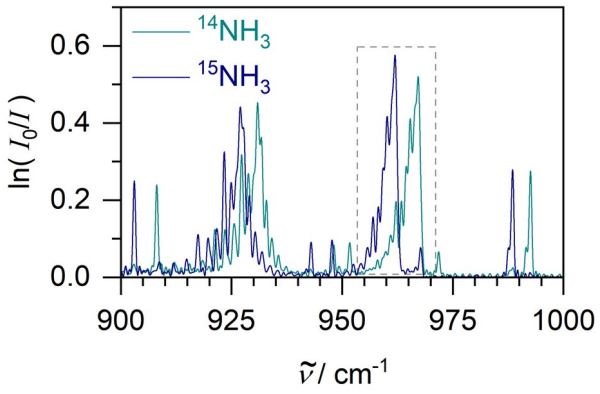

Fig. S17. Experimental White cell FTIR spectra of $^{14}NH_3$ (cyan) and $^{15}NH_3$ (dark blue) gases, each corresponding to 20 mM NH_4^+ in solution. The grey dashed box indicates the ν_2 *Q*-branch fitted for NH_3 analysis.

Fig. **S17** shows typical experimental spectra of $^{14}NH_3$ (black) and $^{15}NH_3$ (red) gases, both corresponding to 20 mM ammonium. The two *Q*-branches of ammonia's ν_2 N-H wagging fundamental are visible, it is centred around 950 cm^{-1} for $^{14}NH_3$. Two *Q*-branches are observed due to the inversion doubling phenomenon exhibited by trigonal pyramidal molecules like ammonia. The ν_2 *P*- and *R*- branches extend over 700 - 1200 cm^{-1}, outside the range displayed for the spectra. The ν_2 band is the strongest in ammonia's IR spectrum and free from CO_2 and water lines and is commonly used for FTIR analysis of $^{14}N/^{15}N$ ammonia. We observed the higher energy *Q*-branch, highlighted by

a dashed box for the prior spectra, to be the most intense ammonia spectral feature so it was utilised for analysis. A self-written computer programme implements the least-squares fit of the 955 - 970 cm^{-1} region of an experimental FTIR spectrum to the sum of scaled $^{14}NH_3$ and $^{15}NH_3$ model spectra and a linear baseline.

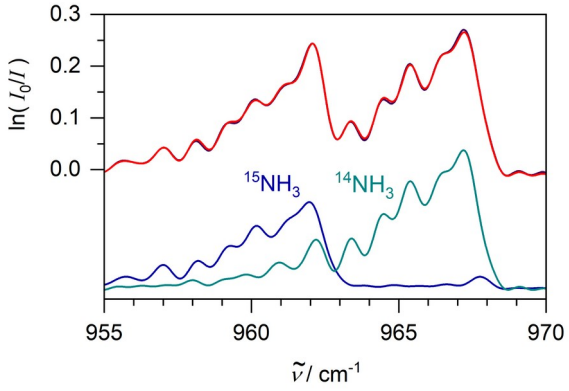

Fig. S18. In black, an experimental White cell FTIR spectrum of $^{14}NH_3$ and $^{15}NH_3$ gases corresponding to 12.5 mM $^{14}NH_4^+$ and 8.25 mM $^{15}NH_4^+$. In red, the sum of the fitted $^{14}NH_3$ and $^{15}NH_3$ models shown below the overlaid spectra.

Fig. **S18** is an example least-squares fit for $^{14}NH_3$ and $^{15}NH_3$. Calibration plots were constructed (shown below in Fig. **S19**) to convert the multipliers of the model spectra (*x*') into concentrations. The model NH_3 spectra were constructed from experimental spectra.

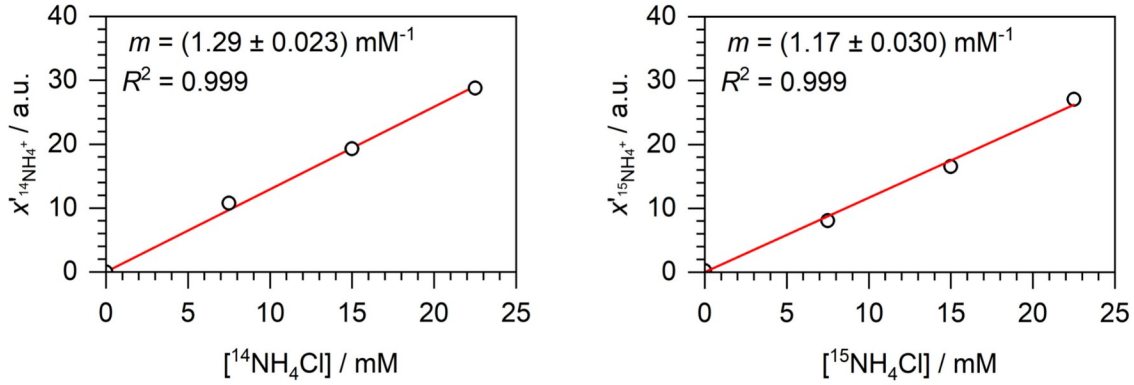

Fig. S19. Calibration plots for $^{14}NH_3$ and $^{15}NH_3$.

Under our conditions, we obtained a dynamic range up to 22.5 mM and a noise equivalent detection limit (1 σ) of 0.13 mM. This was suitable for our bacterial culture samples containing 18 mM $^{14}NH_4^+$ and 10 mM $^{15}NO_3^-$ at the start. $^{14}NH_4^+$ concentrations can only decrease due to biomass synthesis and $^{15}NH_4^+$ concentrations produced cannot exceed that of the 10 mM $^{15}NO_3^-$ supplied.

S.7. References

1. Stewart, V. Nitrate respiration in relation to facultative metabolism in enterobacteria. *Microbiol. Rev.* **1988**, *52*, 190-232, https://doi.org/10.1128/mr.52.2.190-232.1988
2. Bonnefoy, V.; Demoss, J. A. Nitrate reductases in *Escherichia coli*. *Antonie van Leeuwenhoek*. **1994**, *66*, 47-56, https://doi.org/10.1007/BF00871632
3. Stewart, V.; Lu, Y.; Darwin, A. J. Periplasmic nitrate reductase (NapABC enzyme) supports anaerobic respiration by *Escherichia coli* K-12. *J. Bacteriol.* **2002**, *184*, 1314-1323, https://doi.org/10.1128/JB.184.5.1314-1323.2002
4. Wang, H.; Tseng, C. P.; Gunsalus, R. P. The *napF* and *narG* Nitrate Reductase Operons in *Escherichia coli* Are Differentially Expressed in Response to Submicromolar Concentrations of Nitrate but Not Nitrite. *J. Bacteriol.* **1999**, *181*, 5303-5308, https://doi.org/10.1128/JB.181.17.5303-5308.1999
5. Cole, J. Nitrate reduction to ammonia by enteric bacteria: redundancy, or a strategy for survival during oxygen starvation? *FEMS Microbiol. Lett.* **1996**, *136*, 1-11, https://doi.org/10.1016/0378-1097(95)00480-7
6. Chang, L.; Wei, L. I.; Audia, J. P.; Morton, R. A.; Schellhorn, H. E. Expression of the *Escherichia coli* NRZ nitrate reductase is highly growth phase dependent and is controlled by RpoS, the alternative vegetative sigma factor. *Mol. Microbiol.* **2002**, *34*, 756-766, https://doi.org/10.1046/j.1365-2958.1999.01637.x
7. Wang, H.; Gunsalus, R. P. The *nrfA* and *nirB* Nitrite Reductase Operons in *Escherichia coli* Are Expressed Differently in Response to Nitrate than to Nitrite. *Genet. Mol. Biol.* **2000**, *182*, 5813-5822, https://doi.org/10.1128/jb.182.20.5813-5822.2000
8. Smith, M. S. Nitrous oxide production by *Escherichia coli* is correlated with nitrate reductase activity. *Appl. Environ. Microbiol.* **1983**, *45*, 1545-1547, https://doi.org/10.1128/AEM.45.5.1545-1547.1983
9. Metheringham, R.; Cole, J. A. A reassessment of the genetic determinants, the effect of growth conditions and the availability of an electron donor on the nitrosating activity of *Escherichia coli* K-12. *Microbiol.* **1997**, *143*, 2647-2656, https://doi.org/10.1099/00221287-143-8-2647
10. Gilberthorpe, N. J.; Poole, R. K. Nitric oxide homeostasis in *Salmonella typhimurium*. *J. Biol. Chem.* **2008**, *283*, 11146-11154, https://doi.org/10.1074/jbc.M708019200
11. Vine, C. E.; Purewal, S. K.; Cole, J. A. NsrR-dependent method for detecting nitric oxide accumulation in the *Escherichia coli* cytoplasm and enzymes involved in NO production. *FEMS Microbiol. Lett.* **2011**, *325*, 108-114, https://doi.org/10.1111/j.1574-6968.2011.02385.x
12. Vine, C. E.; Cole, J. A. Nitrosative stress in *Escherichia coli*: reduction of nitric oxide. *Biochem. Soc. Trans.* **2011**, *39*, 213-215, https://doi.org/10.1042/BST0390213
13. Corker, H.; Poole, R. K. Nitric Oxide Formation by *Escherichia coli*: Dependence On Nitrite Reductase, The NO-Sensing Regulator Fnr, and Flavohemoglobin Hmp. *J. Biol. Chem.* **2003**, *278*, 31584-31592, https://doi.org/10.1074/jbc.M303282200
14. Gardner, A. M.; Helmick, R. A.; Gardner, P. R. Flavorubredoxin, an Inducible Catalyst for Nitric Oxide Reduction and Detoxification in *Escherichia coli*. *J. Biol. Chem.* **2002**, *277*, 8172-8177, https://doi.org/10.1074/jbc.M110471200
15. Wang, J.; Vine, C. E.; Balasiny, B. K.; Rizk, J.; Bradley, C. L.; Tinajero-Trejo, M.; Poole, R. K.; Bergaust, L. L.; Bakken, L. R.; Coole, J. A. The role of the hybrid cluster protein, Hcp and its reductase, Hcr, in high affinity nitric oxide reduction that protects anaerobic cultures of *Escherichia coli* against nitrosative stress. *Mol. Microbiol.* **2016**, *100*, 877-892, https://doi.org/10.1111/mmi.13356

16. Weiss, B. Evidence for Mutagenesis by Nitric Oxide during Nitrate Metabolism in *Escherichia coli*. *J. Bacteriol.* **2006**, *188*, 829-833, https://doi.org/10.1128/JB.188.3.829-833.2006
17. Poock, S. R.; Leach, E. R.; Moir, J. W. B.; Cole, J. A.; Richardson, D. J. Respiratory Detoxification of Nitric Oxide by the Cytochrome *c* Nitrite Reductase of *Escherichia coli*. *J. Biol. Chem.* **2002**, *277*, 23664-23669, https://doi.org/10.1074/jbc.M200731200
18. Kim, S. O.; Orii, Y.; Lloyd, D.; Hughes, M. N.; Poole, R. K. Anoxic function for the *Escherichia coli* flavohaemoglobin (Hmp): reversible binding of nitric oxide and reduction to nitrous oxide. *FEBS Lett.* **1999**, *445*, 389-394, https://doi.org/10.1016/S0014-5793(99)00157-X
19. Kaldorf, M.; Linne von Berg, K. H.; Meier, U.; Servos, U.; Bothe, H. The reduction of nitrous oxide to dinitrogen by *Escherichia coli*. *Arch. Microbiol.* **1993**, *160*, 432-439, https://doi.org/10.1007/BF00245303
20. Metcalfe, G. D.; Smith, T. W.; Hippler, M. On-line analysis and in situ pH monitoring of mixed acid fermentation by *Escherichia coli* using combined FTIR and Raman techniques. *Anal. Bioanal. Chem.* **2020**, *412*, 7303-7319, https://doi.org/10.1007/s00216-020-02865-5
21. Sharpe, S. W.; Johnson, T. J.; Sams, R. L.; Chu, P. M.; Rhoderick, G. C.; Johnson, P. A. Gas-Phase Databases for Quantitative Infrared Spectroscopy. *Appl. Spectrosc.* **2004**, *58*, 1452-1461, https://doi.org/10.1366/0003702042641281
22. Salter, R.; Chu, J.; Hippler, M. Cavity-enhanced Raman spectroscopy with optical feedback cw diode lasers for gas phase analysis and spectroscopy. *Analyst.* **2012**, *137*, 4669-4676, https://doi.org/10.1039/c2an35722d
23. Hippler, M. Cavity-Enhanced Raman Spectroscopy of Natural Gas with Optical Feedback cw-Diode Lasers. *Anal. Chem.* **2015**, *87*, 7803-7809, https://doi.org/10.1021/acs.analchem.5b01462
24. Smith, T. W.; Hippler, M. Cavity-Enhanced Raman Spectroscopy in the Biosciences: *In situ*, Multicomponent, and Isotope Selective Gas Measurements To Study Hydrogen Production and Consumption by *Escherichia coli*. *Anal. Chem.* **2017**, *89*, 2147-2154, https://doi.org/10.1021/acs.analchem.6b04924
25. Metcalfe, G. D.; Alahmari, S.; Smith, T. W.; Hippler, M. Cavity-Enhanced Raman and Helmholtz Resonator Photoacoustic Spectroscopy to Monitor the Mixed Sugar Metabolism of *E. coli*. *Anal. Chem.* **2019**, *91*, 13096-13104, https://doi.org/10.1021/acs.analchem.9b03284
26. Mohr, C.; Spencer, C. L.; Hippler, M. Inexpensive Raman Spectrometer for Undergraduate and Graduate Experiments and Research. *J. Chem. Educ.* **2010**, *87*, 326-330, https://doi.org/10.1021/ed800081t
27. Ryabenkova, Y.; Jadav, N.; Conte, M.; Hippler, M.; Reeves-McLaren, N.; Coates, P. D.; Twigg, P.; Paradkar, A. Mechanisms of Hydrogen-Bonded Complex Formation between Ibuprofen and Nanocrystalline Hydroxyapatite. *Langmuir.* **2017**, *33*, 2965-2976, https://doi.org/10.1021/acs.langmuir.6b04510